Supporting Information

NiS_2 nanoboxes wrapped in carbon with a core-shell structure for high-performance sodium storage

Li Wang[a], Ying Zhu[a], Dong Yan[a], Jingjing Wang[a], Rui Wu[a], Jinxia Jiang[b], Xiaobin Niu[a], Chia-Yun Chen[c], Hanchao Li[a]*, Jun Song Chen[a,d,e]**

[a]School of Materials and Energy, University of Electronic Science and Technology of China, Chengdu, 610054, China. Email: jschen@uestc.edu.cn; lhc@uestc.edu.cn.

[b]Chongqing Medical and Pharmaceutical College, Chongqing 401331, China. Email: 2020364@cqmpc.edu.cn.

[c]Department of Materials Science and Engineering, National Cheng Kung University, Tainan, 70101, Taiwan.

[d]Institute for Advanced Study, Chengdu University, Chengdu 610106, China.

[e]Shenzhen Institute for Advanced Study, University of Electronic Science and Technology of China, Shenzhen, China.

Experimental section

Synthesis of Ni-based metal organic compound (Ni-MOC) nanoparticles

First, 1.152 g of nickel (II) acetate tetrahydrate and 3.15 g of polyvinylpyrrolidone (PVP, with a molecular weight of 58,000) were added to 180 ml of anhydrous ethanol at room temperature. The mixture was then stirred for 30 minutes to ensure complete dissolution. Subsequently, the solution was transferred to an oil bath at a temperature of 85 °C and stirred for 24 hours. After that, the green precipitate of Ni-MOC was isolated through centrifugation. The obtained precipitate was collected, washed thrice with ethanol, and subsequently dried at 60 °C.

Synthesis of Ni-MOC@PAN

412 mg of as-synthesized Ni-MOC powder was dispersed in 2.5 ml of dimethylformamide (DMF) solvent by ultrasonic treatment. Then, 206 mg of Polyacrylonitrile (PAN, with a molecular

weight of 150,000) was added to the solution and stirred at room temperature for 48 hours to ensure complete dissolution. During the electrospinning process, the distance between the nozzle and the aluminum foil was kept at 12 cm, and the nozzle was driven by a 13 kV voltage at a stable filamentation speed of 0.03 mm min^{-1}, resulting in the formation of Ni-MOC@PAN. Under the same experimental conditions, the ratio of Ni-MOC-to-PAN was varied, specifically set to 1:1 and 3:1 respectively.

Synthesis of NiS_2@N-C

The as-obtained Ni-MOC@PAN composite was placed downstream of a ceramic boat, and a specific amount of sulfur powder (mass ratio between Ni-MOC@PAN: sulfur powder = 1:5) was added upstream. The ceramic boat was then positioned in a tube furnace and heated in an argon atmosphere at a rate of 1°C min^{-1} until reaching 450 °C, and maintained for 3 hr to facilitate the sulfidation reaction. The resulting product obtained was the NiS_2@N-C composite. Under the same experimental conditions, the sulfidation temperatures were altered, being set at 600 °C and 750 °C, respectively.

Synthesis of Pure NiS_2

Under the same experimental conditions, Ni-MOC was directly sulfurized to produce pure NiS_2.

Synthesis of N-C

In the Ni-MOC@PAN synthesis conditions mentioned above, pure PAN fibers were obtained without the addition of Ni-MOC powder, which were then carbonized using the above conditions.

Material Characterization

X-ray diffractometer (XRD, Malvern Panalytical) was used to analyze the chemical phase of the samples. The morphological and microstructural examinations were carried out using scanning electron microscopy (SEM, Phenom Pharos) and transmission electron microscopy (TEM, JEM2010F). The chemical state of the samples was determined by X-ray photoelectron spectroscopy (XPS, Thermo Scientific K-Alpha). The carbon content in the samples was analyzed using a thermogravimetric analyzer (TGA, NETZSCH STA 449F5), and surface texture of the samples were measured by the nitrogen adsorption/desorption isotherms using a surface analyzer (Kubo-X1000).

Electrochemical measurement

For the fabrication of the electrodes, the active material, Super P conductive agent, and PVDF binder were mixed in a mass ratio of 7:2:1 and stirred evenly. The mixed slurry was then spread

evenly on a copper foil and dried overnight in a vacuum environment at 80 °C. The half-cell was assembled using a CR2025 coin cell casing within an argon-filled glove box, with water and oxygen levels maintained below 1 ppm. Metallic sodium and glass fiber (Whatman) were used as the anode and separator, respectively, with 1 M $NaPF_6$ in dimethyl ether (DME) as the electrolyte. The mass loading of active material in each electrode ranged from 0.8 to 1.2 mg cm^{-2}. Charge-discharge tests and CV analysis were carried out within a voltage range of 0.01-3.0 V (vs. Na/Na^+) at varying current densities and different scan rates, respectively. Furthermore, EIS measurements were performed across a frequency range of 0.01-10^5 Hz using a Bio-Logic SP-150 electrochemical workstation.

Theoretical Calculation

Utilizing Density Functional Theory (DFT) in conjunction with the Vienna Ab initio Simulation Package (VASP), developed at the University of Vienna, Austria, first-principles calculations were performed. Within the framework of the Generalized Gradient Approximation (GGA), the Perdew-Burke-Ernzerhof (PBE) approach was employed to elucidate the interactions among electrons. To address the strong electron interactions in the 3d orbitals of transition metals, we introduced the DFT+U method in our calculations and performed spin-polarized treatment. The U-J difference for nickel (Ni) was set to 6.4 electron volts. The (200) crystal plane of cubic NiS_2 along with a single-layer carbon network was selected to construct a heterostructure model. To eliminate the untrue interaction effect, we set a vacuum layer thickness of 15 angstroms in the model. The adsorption energy of Na^+ (ΔE_{ads}) was defined as:

$$E_{ads} = E_{total} - E_{base} - E_{Na}$$

where E_{total} is the total energy of the substrate adsorbed with Na^+, while E_{base} and E_{Na} are the energy of the substrate and Na^+, respectively.

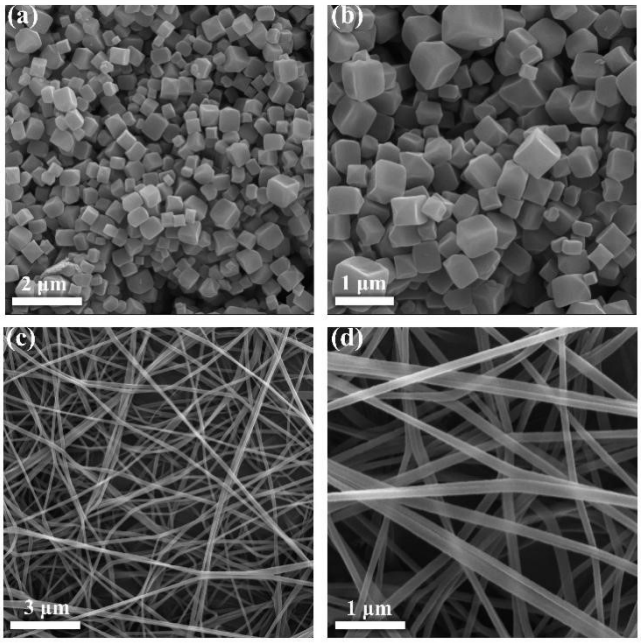

Figure S1. SEM images of (a-b) Ni-MOC and (c-d) pure PAN fibers.

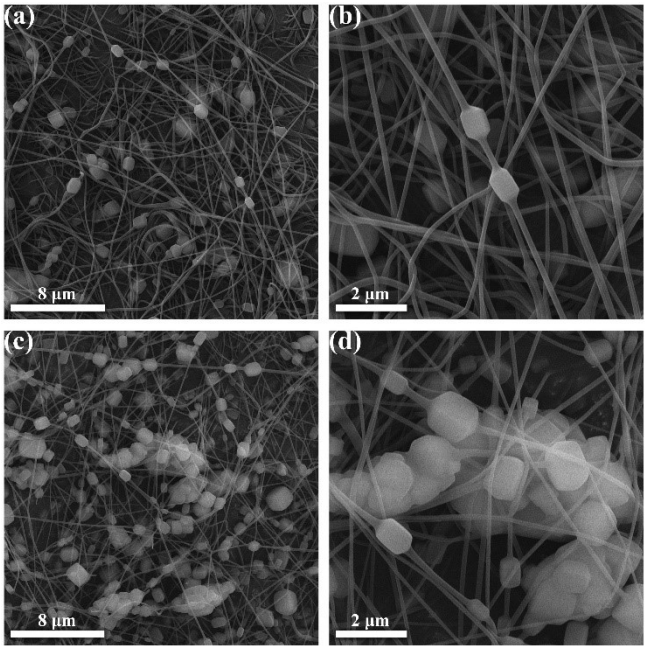

Figure S2. SEM images of samples prepared with different Ni-MOC-to-PAN ratio: (a-b) 1:1 and (c-d) 3:1.

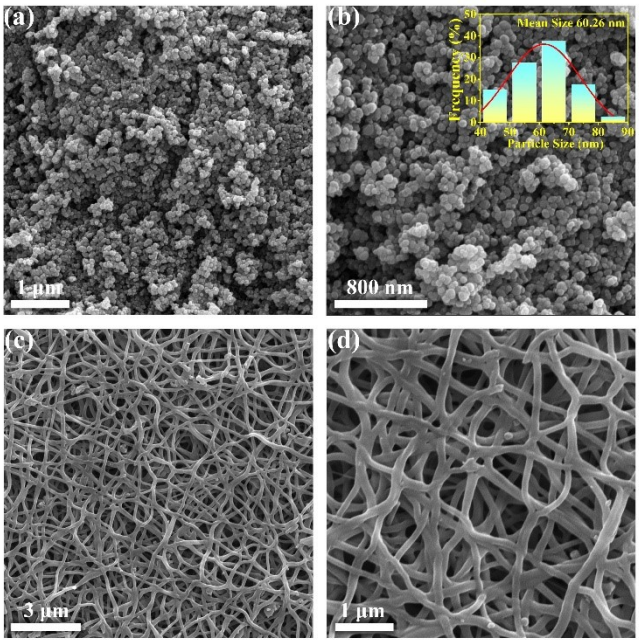

Figure S3. (a-b) SEM images of Pure NiS_2 and the size distribution diagrams of pure NiS_2 nanoparticles. (c-d) SEM images of N-C after sulfurization.

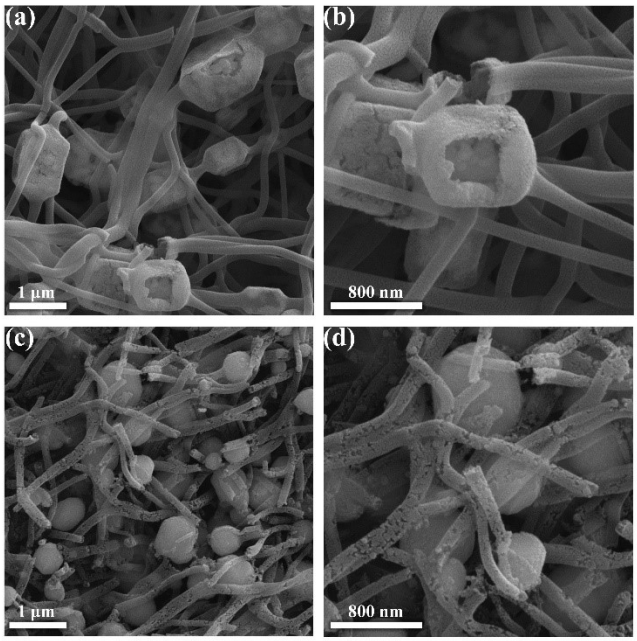

Figure S4. SEM images of the sample prepared at different carbonization temperatures: (a-b) 600 °C and (c-d) 750 °C.

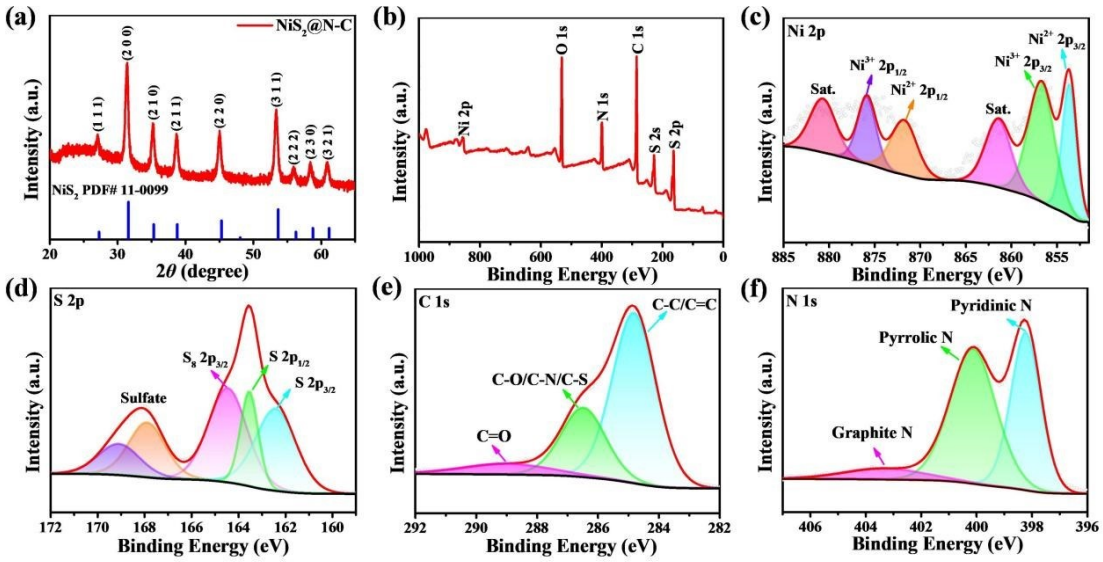

Figure S5. (a) XRD patterns of as-prepared NiS_2@N-C. (b) XPS survey spectrum of NiS_2@N-C. (c) Ni 2p. (d) S 2p. (e) C 1s. (f) N 1s spectra.

The high-resolution Ni 2p spectrum in Figure S5c reveals the orbital peaks corresponding to Ni^{2+} $2p_{1/2}$, Ni^{2+} $2p_{3/2}$, Ni^{3+} $2p_{1/2}$, and Ni^{3+} $2p_{3/2}$ are observed at 871.88, 853.68, 875.88, and 856.78 eV, respectively. The presence of the Ni^{3+} may be attributed to the oxidation of some Ni^{2+} in the material to Ni^{3+}. Furthermore, two typical satellites are observed at 861.48 and 880.78 eV.[1] For the S 2p spectrum of NiS_2@N-C shown in Figure S5d, the two primary peaks at 162.48 and 163.58 eV correspond to S $2p_{3/2}$ and S $2p_{1/2}$, respectively, demonstrating the existence of the Ni─S bond.[2] Moreover, the peak at 164.48 eV is associated with the S─S bond of α-S_8, indicating the possible presence of residual S during the sulfurization process. The peaks at 168.4 and 169.5 eV are associated with S─O and sulfate bonds, respectively.[3] In Figure S5e, the C 1s spectrum exhibits three distinct peaks at 284.78, 286.48, and 289.08 eV, corresponding to the C─C/C=C bond, the C─O/C─N/C─S bond, and the C=O bond, respectively. In Figure S5f, the observed peaks at 398.28, 399.98, and 403.38 eV in the N 1s spectrum can be attributed to three different nitrogen species: pyridinic N, pyrrolic N, and graphitic N, respectively.[4] The nitrogen doping not only serves to increase the presence of defects, creating additional active sites for Na^+ insertion, but also contributes to a further enhancement of the electrical conductivity within the carbon matrix.

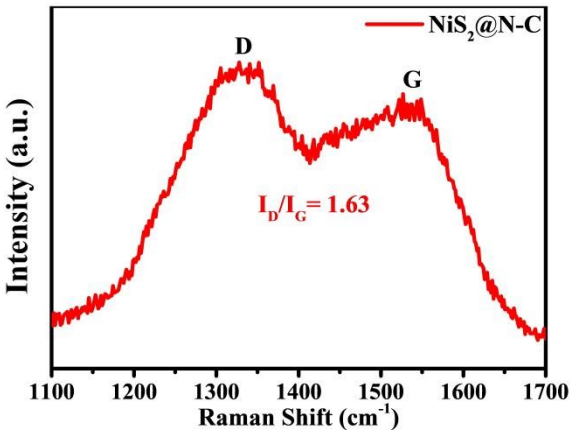

Figure S6. Raman spectrum of NiS_2@N-C.

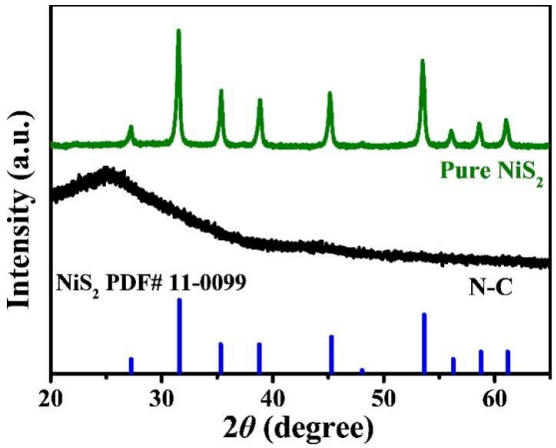

Figure S7. XRD patterns of Pure NiS2 and N-C.

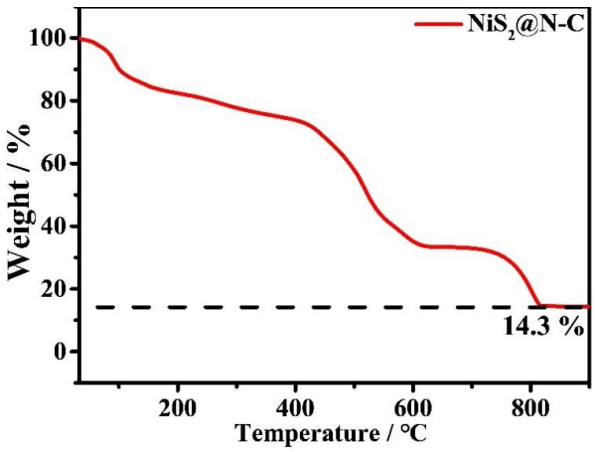

Figure S8. TGA analysis of NiS_2@N-C. Based on the follow equation:[5] $2NiS_2(s) + C(s) + 6O_2(g) = 2NiO(s) + 4SO_2(g) + CO_2(g)$. It can be inferred that only NiO was left after the TGA test, with a residual mass of 14.3% at 900 °C. Therefore, the content of NiS_2 can be calculated as follows: $14.3\% \times M_{NiS2} \div M_{NiO} = 23.5\%$, and accordingly, the N-C content is determined to be 76.5%.

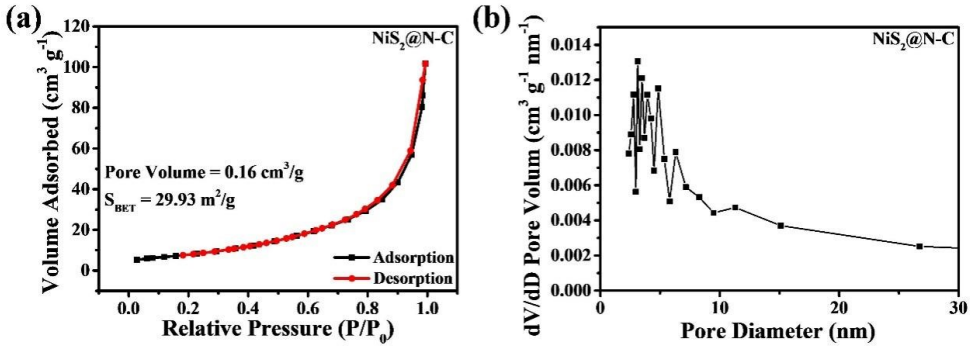

Figure S9. (a) The nitrogen adsorption–desorption isotherm, and (b) the corresponding pore size distribution of NiS_2@N-C.

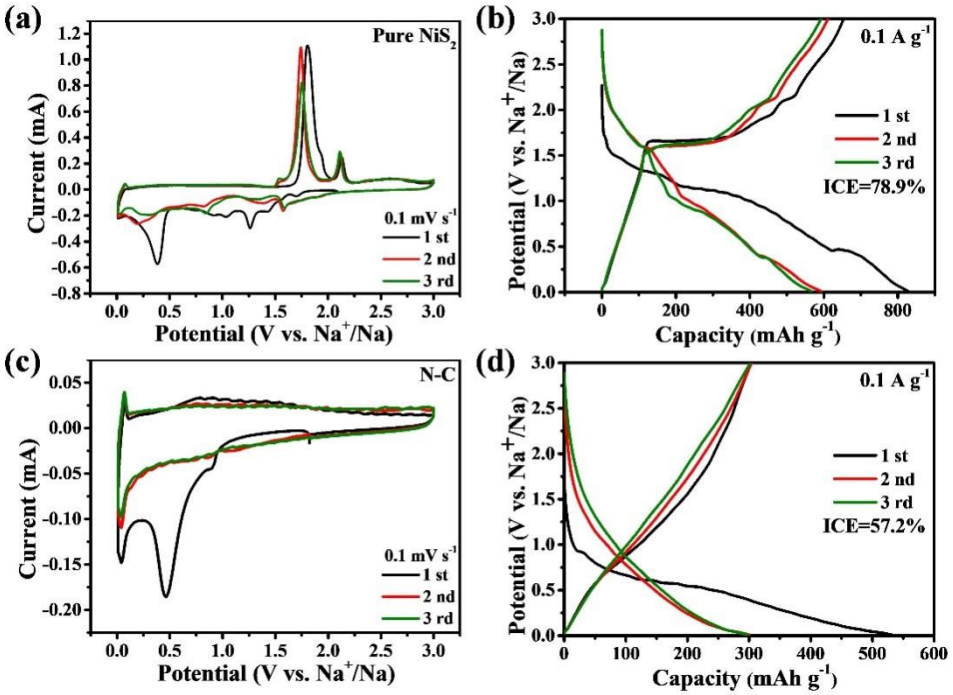

Figure S10. (a) CV curves of Pure NiS_2 at 0.1 mV s^{-1} and (b) Charge and discharge curves of Pure NiS_2 at 0.1 A g^{-1}. (c) CV curves of N-C at 0.1 mV s^{-1} and (d) Charge and discharge curves of N-C at 0.1 A g^{-1}.

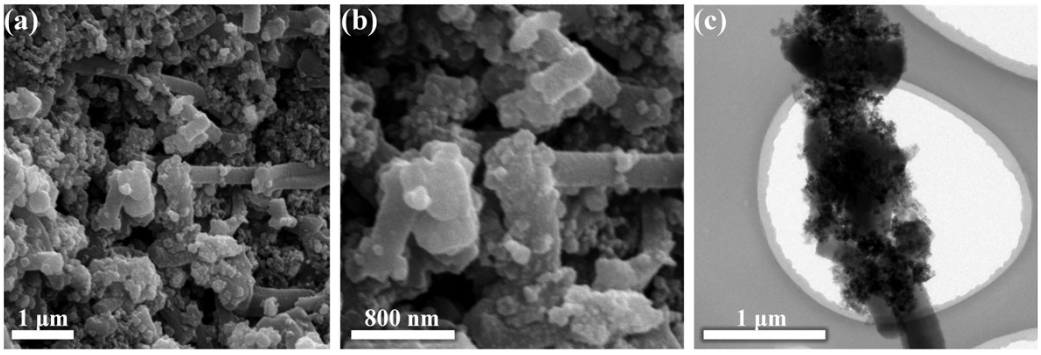

Figure S11. (a-b) SEM images, and (c) TEM images of NiS_2@N-C electrode after 900 cycles at a current density of 5 A g^{-1}.

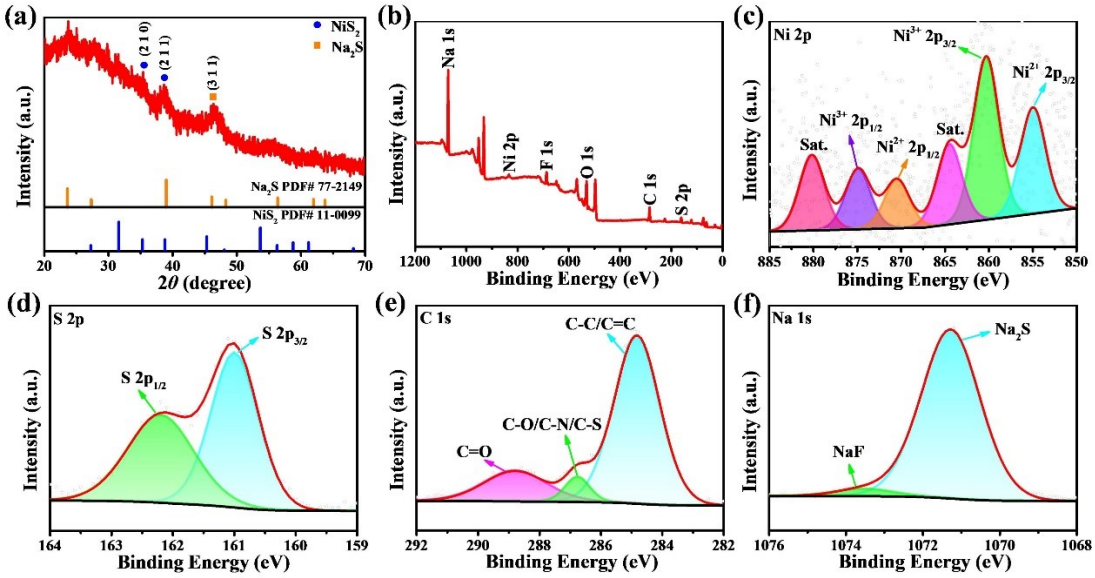

Figure S12. (a) XRD patterns of as-prepared NiS_2@N-C electrode after 900 cycles at a current density of 5 A g^{-1}. (b) XPS survey spectrum of NiS_2@N-C electrode after 900 cycles at a current density of 5 A g^{-1}. (c) Ni 2p. (d) S 2p. (e) C 1s. (f) Na 1s spectra.

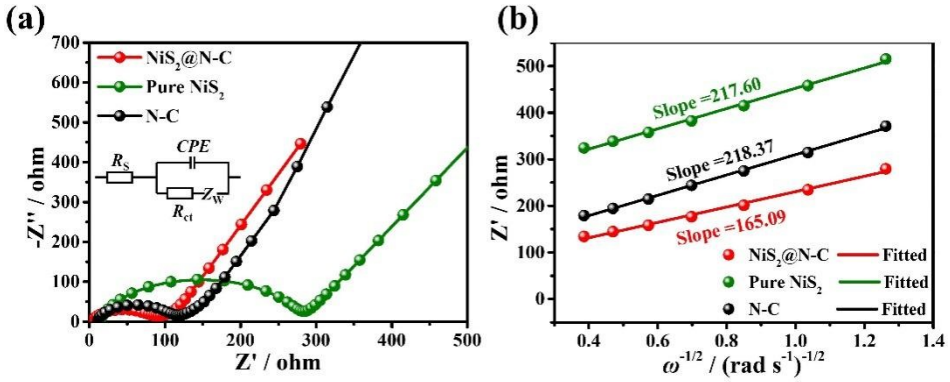

Figure S13. (a) EIS curves of different samples before cycling measurements and (b) the corresponding relationship between $\omega^{-1/2}$ and Z' in the low-frequency region.

The Nyquist plots obtained before cycling measurements are displayed in Figure S13a. The charge transfer resistance (*R*ct) value of NiS_2@N-C (76.1 Ω) is significantly smaller than that of Pure NiS_2 (268.2 Ω) and N-C (92.2 Ω). This further indicates that the 3D conductive network of NiS_2@N-C significantly enhances electrical conductivity. Moreover, the Warburg factor σ is determined by plotting the slope of the fitted line of Z' versus $\omega^{-1/2}$, as depicted in Figure S13b. The diffusion coefficient of Na^+ (D_{Na+}) in the electrode material can be determined using the following formula:[6]

$$D_{Na^+} = \frac{R^2T^2}{2n^4F^4S^2C^2\sigma^2}$$

Where *R* represents the gas constant, *T* denotes the absolute temperature, *n* represents the number

of electron transfers, *F* signifies the Faraday constant, *S* stands for the electrode surface area and *C* denotes the concentration of sodium ions in the electrolyte.

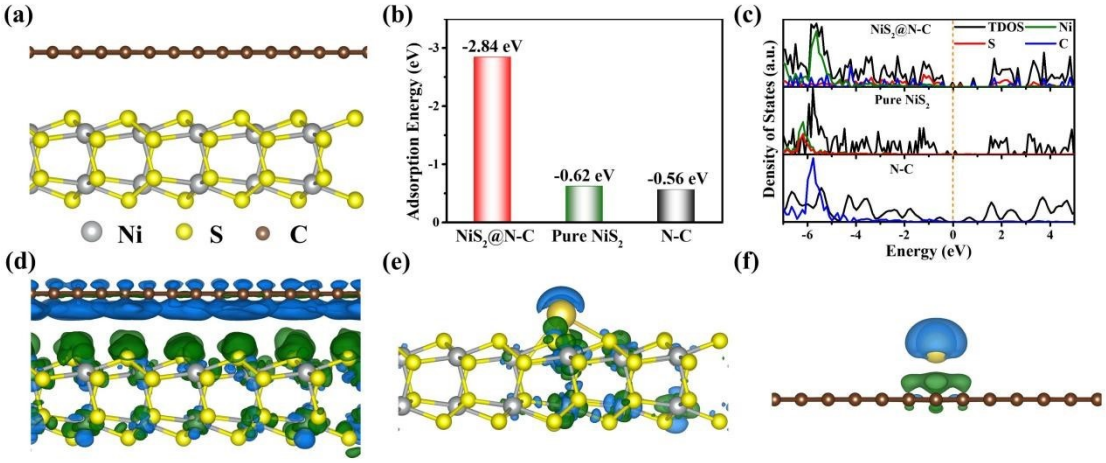

Figure S14. DFT calculations of three distinct models: (a) Structural model of NiS_2@N-C. (b) Sodium ion adsorption energies. (c) The DOS and (d-f) differential charge distribution map of NiS_2@N-C, Pure NiS_2 and N-C. The green part represents charge accumulation, and the blue region represents charge depletion.

Figure S14b presents the adsorption energies of NiS_2@N-C, Pure NiS_2 and N-C for Na^+, which are -2.84 eV, -0.62 eV, and -0.56 eV, respectively. The results indicate that the adsorption energy of NiS_2@N-C for Na^+ is significantly higher than that of Pure NiS_2@N-C and N-C, suggesting that NiS_2@N-C has a stronger affinity in the process of sodium ion adsorption. By calculating and analyzing the density of states (DOS) for three models (Figure S14c), we found that the heterostructure NiS_2@N-C exhibits a higher charge density near the Fermi level compared to both Pure NiS_2 and N-C, resulting in superior electrical conductivity. Furthermore, in Figure S14d, the differential charge density map of the NiS_2@N-C model illustrates the phenomenon of electron redistribution in the interface region (Figure S14e-f present the differential charge density map of Pure NiS_2 and N-C model, respectively). Specifically, a positive charge accumulation is observed on the NiS_2 side, while negative charge accumulation occurs on the N-C side. This charge redistribution arises from the interaction between NiS_2 and N-C. Notably, the polarity of the Ni─S bond facilitates electron transfer from Ni to S, and the conductivity of N-C promotes both migration and distribution of electrons.[7, 8]

Table S1. Comparison of the performance of different NiS_2-based anode materials.

Materials	Potential range (V)	Rate performance		Cycling performance			Reference
		Current density (A g^{-1})	Capacity (mAh g^{-1})	Current density (A g^{-1})	Cycles	Retention (mAh g^{-1})	
NiS_2@N-C	**0.01-3**	**5**	**444**	**1/5**	**300/900**	**585/486**	**This work**
NiS_2@C@C	0.01-3	1.6	448	0.1	100	581	**9**
NiS_2@NC	0.005-3	3	294	0.1/0.5	100/300	506/356	**10**
Hollow NiS_2@G	0.005-3	2	528	1	300	530	**11**
MoS_2/NiS_2	0.2-3	5	375	1	350	481	**12**
NiS_2/NG	0.01-2.6	2	545	0.5/2	1200/100	590/545	**13**
Ni@NCNTs HMs	0.2-3	5	333	1	500	345	**2**
NiS_2	0.4-2.9	5	253	0.5	1000	319	**14**
$NiS_2/Ti_3C_2T_x$	0.01-3	2	147	1	800	179	**15**
NiS_2/rGO	0-3	10	320	5	500	308	**16**
$ReS_2@NiS_2$	0-3	5	230	1	220	400	**17**
NiS_2@MWCNTs	0.01-3	2	382	0.2/1	400/600	464/419	**18**
NiS_2@rGO	0.2-2.8	5	324	1	1800	378	**19**
NiS_2NP/p-CNF	0.01-3	2	300	2	1000	200	**20**
NiS_2/N,S-rGO	0.01-3	1	205	0.1	200	208	**21**
CoS_2/NiS_2-RGO	0.01-3	0.5	58	0.1	200	127	**22**

References

1 B. Huang, J. Yuan, Y. Lu, Y. Zhao, X. Qian, H. Xu, G. He and H. Chen, *Chem. Eng. J.*, 2022, **436**, 135231.

2 B. Cong, X. Li and G. Chen, *Chem. Eng. J.*, 2023, **460**, 141713.

3 L. Lin, K. Wang, A. Sarkar, C. Njel, G. Karkera, Q. Wang, R. Azmi, M. Fichtner, H. Hahn, S. Schweidler and B. Breitung, *Adv. Energy Mater.*, 2022, **12**, 2103090.

4 Zulkifli, S. Lee, G. Alfaza, A. N. Fahri, B. Sambandam, V. Mathew, S. Lee, J. Park, M. Song, J. Lee, J. Y. Hwang and J. Kim, *Mate. Today Sustain.*, 2023, **22**, 100348.

5 S.-L. Yang, H.-B. Yao, M.-R. Gao and S.-H. Yu, *CrystEngComm*, 2009, **11**, 1383-1390.

6 P. Wang, J. Huang, J. Zhang, L. Wang, P. Sun, Y. Yang and Z. Yao, *J. Mater. Chem. A*, 2021, **9**, 7248-7256.

7 F. Chen, S. J. Robertson, X. Xu, S. Chen, C. Sun, M. Shao and J. Wang, *Nano Energy*, 2024, **123**, 109414.

8 F. He, X. Chen, Y. Xue and Y. Li, *Angew. Chem. Int. Ed. Engl.*, 2024, **63**, e202318080.

9 G. Zhao, Y. Zhang, L. Yang, Y. Jiang, Y. Zhang, W. Hong, Y. Tian, H. Zhao, J. Hu, L. Zhou, H. Hou, X. Ji and L. Mai, *Adv. Funct. Mater.*, 2018, **28**, 1803690.

10 J. Li, J. Li, D. Yan, S. Hou, X. Xu, T. Lu, Y. Yao, W. Mai and L. Pan, *J. Mater. Chem. A*, 2018, **6**, 6595-6605.

11 R. Bi, C. Zeng, H. Huang, X. Wang and L. Zhang, *J. Mater. Chem. A*, 2018, **6**, 14077-14082.

12 Y. Zhang, B. Han, Q. Gao, Z. Cai, C. Zhou, G. Hu, J. Li and R. Sun, *Nano Energy*, 2024, **128**, 109941.

13 S. Luo, J. Shang, Y. n. Xu, H. Cheng, L. Zhang and Y. Tang, *Adv. Funct. Mater.*, 2024, **34**, 2403166.

14 R. Sun, S. Liu, Q. Wei, J. Sheng, S. Zhu, Q. An and L. Mai, *Small*, 2017, **13**, 1701744.

15 W. X. Zhang, J. H. Zhang, Y. K. Zhang, C. He and P. Zhao, *Ionics*, 2022, **28**, 4621-4629.

16 H. Zheng, X. Chen, L. Li, C. Feng and S. Wang, *Mater. Res. Bull.*, 2021, **142**, 111430.

17 Z. Cai, Z. Peng, X. Liu, R. Sun, Z. Qin, H. Fan and Y. Zhang, *Chin. Chem. Lett.*, 2021, **32**, 3607-3612.

18 W. X. Zhang, Z. Li, J. H. Zhang, C. He and X. H. Ning, *J. Alloys Compd.*, 2024, **971**, 172669.

19 J. Cai, X. Chen, X. Duan, G. Yang, Q. Zhang, H. Fan, Z. Liu and F. Peng, *Electrochim. Acta*, 2023, **462**, 142705.

20 W. Zhao, S. Ci, X. Hu, J. Chen and Z. Wen, *Nanoscale*, 2019, **11**, 4688-4695.

21 X. Dong, F. Chen, G. Chen, B. Wang, X. Tian, X. Yan, Y. X. Yin, C. Deng, D. Wang, J. Mao, S. Xu and S. Zhang, *J. Colloid Interface Sci.*, 2022, **619**, 359-368.

22 J. Liu, Y.-G. Xu and L.-B. Kong, *J. Mater. Sci.: Mater. Electron.*, 2020, **31**, 9946-9959.